Performance evaluation of CsI screens for X-ray imaging *

ZHAO Bo-Zhen(赵博震)[1,2,3] QIN Xiu-Bo(秦秀波)[1,2;1)] FENG Zhao-Dong(冯召东)[1,2,3]
WEI Cun-Feng(魏存峰)[1,2] CHEN Yan(陈研)[4] WANG Bao-Yi(王宝义)[1] WEI Long(魏龙)[1,2]

[1] Key Laboratory of Nuclear Radiation and Nuclear Energy Technology, Institute of High Energy Physics, Chinese Academy of Sciences, Beijing 100049, China
[2] Beijing Engineering Research Center of Radiographic Techniques and Equipment, Beijing 100049, China
[3] University of Chinese Academy of Sciences, Beijing 100049, China
[4] Chongqing Zhence Science and Technology Corporation Limited, Chongqing 400044, China

Abstract: CsI film has been one of the most extensively used scintillators for indirect X-ray imaging because of its needle-like micro-structure. The purpose of this paper is to investigate the imaging performance of CsI screen as a function of thickness and radiation quality. Four multilayer scintillation screens with microcolumnar CsI:Tl film (thicknesses of 50 μm, 100 μm, 200 μm and 300 μm) included were prepared and coupled to an optical imaging sensor. The modulation transfer function (MTF), normalized noise power spectrum (NNPS) and detective quantum efficiency (DQE) of these screens were evaluated based on the standard IEC 62220-1, and the results indicated that, in the medium spatial frequency range (1–6 lp/mm), the MTF of CsI screens with the same thickness was lower when the incident X-ray photon energy was higher, possibly owing to scattering and K-fluorescence re-absorption effects. The NNPS in the higher spatial frequency range (above 8 lp/mm) is dominated by stochastic noise while the entrance surface air Kerma (ESAK) decreases. For 100 μm, 200 μm and 300 μm thick CsI screens, the DQE under RQA7 and RQA9 is lower than that under RQA3 and RQA5 due to low absorption efficiency.

Key words: microcolumnar CsI:Tl film, scintillation screen, DQE

PACS: 29.40.Mc **DOI:** 10.1088/1674-1137/38/11/116003

1 Introduction

X-ray imaging technology has widespread applications in nondestructive testing (NDT) [1], macromolecular crystallography [2], X-ray astronomy [3], synchrotron radiation [4], micro-CT [5], X-ray microscopy [6], and nuclear medical imaging [7]. Cesium Iodide (CsI) screens, consisting of microcolumnar thallium doped cesium iodide (CsI:Tl) film and other accessorial films, have been developed into one of the most desired X-ray converter materials in the last fifty years owing to their microcolumnar structure [8]. This structure helps to reduce depth-dependent blur, and results in the spatial resolution being superior to other X-ray converter materials, such as powder gadolinium oxysulphide (GOS) phosphor [9].

The imaging performance of CsI screens is affected by several factors, such as thickness, structure, substrate and the other accessorial films used. B. Schmitt et al [10] investigated the morphologies of alkali halide films deposited with different structures. It was found that the spatial resolution and signal to noise ratio (SNR) of needle-like structured film was better than other structures. According to the International Electrotechnical Commission (IEC) standard, W. Marshall et al [11] compared the modulation transfer function (MTF), normalized noise power spectrum (NNPS) and detective quantum efficiency (DQE) of several flat-panel detectors used in digital mammography systems. Their results suggested that detectors consisting of microcolumnar CsI:Tl film and a-Si:H had higher DQE, meaning a better overall imaging performance. To study the light channeling process in microcolumnar CsI:Tl film, which contributes to the high spatial resolution of CsI screens, W. Zhao et al [12] measured the Swank factor, MTF, noise power spectrum (NPS) and DQE of fiber optic scintillators (FOS) with various thicknesses, demonstrating that the microcolumnar structure improved spatial resolution significantly. Due to researchers either not being able to manufacture microcolumnar CsI:Tl film or being unwilling to reveal trade secrets, although studies on the imaging performance of CsI screens have been reported, there is a lack of comprehensive physical characterization as a function of thickness and radiation quality.

Received 10 January 2014, Revised 29 April 2014

∗ Supported by National Key Scientific Instrument and Equipment Development Project (2011YQ03011205, 2013YQ03062902) and Basic and Frontier Research Programs (General) Project of Chongqing (CSTC2013JCYJA1640)

1) E-mail: qinxb@ihep.ac.cn

In this article, a series of CsI screens with different film thicknesses were prepared and coupled with an optical imaging sensor. The X-ray imaging metrics, including MTF, NNPS and DQE, were calculated according to a method based on the guidelines published by the IEC [13], which has standardized the methodology for measuring DQE in digital X-ray imaging detectors. The measurement presents X-ray imaging properties of CsI screens with various thicknesses under different radiation conditions. We expect that the results will be beneficial for the design and application of CsI:Tl screens in X-ray imaging detectors.

2 Materials and methods

2.1 Sample preparation

Four CsI screens were fabricated with microcolumnar CsI:Tl film grown on graphite substrate by a thermal evaporation process. Since CsI:Tl is hygroscopic, the surface of each screen was coated with a protective layer to seal the CsI from moisture. This protective layer is a kind of transparent organic film about 8 μm in thickness. As shown in Fig. 1(a), the active area of each screen is 48 mm×48 mm, and the graphite substrate is 50 mm× 50 mm in area with a thickness of 1 mm. The thermal evaporation parameters of each screen were exactly the same, so the morphologies are identical expect for the film thickness, which was 50 μm, 100 μm, 200 μm and 300 μm, respectively. The thicknesses were confirmed by a scanning electron microscope (SEM, HITACHI S4800) test. The cross profile of the microcolumnar CsI:Tl film, with well-oriented columnar growth, is shown in Fig. 1(b). The microcolumns facilitate the channeling of light to promote spatial resolution.

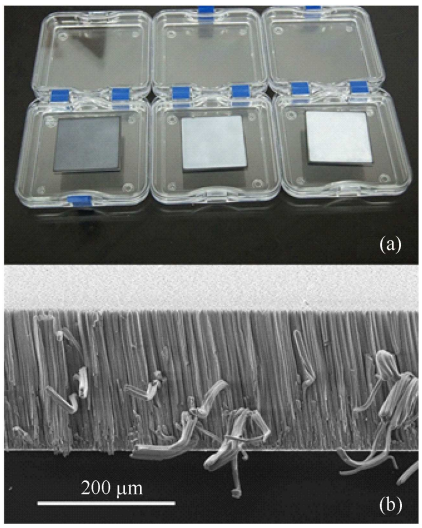

Fig. 1. (a) From left, the CsI screen with 100 μm, 200 μm and 300 μm thick microcolumnar CsI:Tl film, respectively. (b) An SEM image of the broken edge of a microcolumnar CsI:Tl film.

2.2 Detector structure

The CsI screens were coupled with an optical imaging sensor, which consisted of a fiber optic taper (FOT) bonded directly to a charge-coupled device (CCD) chip. The large end of the FOT, coupled with the CsI screen, was 52 mm×52 mm, and the small end, bonded to the CCD chip, was 36 mm×36 mm, so its magnification ratio was 14:9. The FOT fiber diameter was 6 μm at the large end and 3.86 μm at the small end. A CCD was chosen for the imaging due to its remarkable linearity, low dark signal, low read noise and high sensitivity performance [14]. The CCD chip used in the optical imaging sensor was a TURESENSE KAF-16803, which has a pixel size of 9 μm×9 μm and 4096 × 4096 active pixels, so the corresponding active area is 36.86 mm×36.86 mm. Combining the pixel size of the CCD and the magnification ratio of the FOT, the effective pixel size of the optical imaging sensor was 13 μm×13 μm. There are two pronounced advantages for this structure of optical imaging sensor. First, compared to the fragile surface of a CCD, on which it is risky to attach a CsI screen directly, handling the surface of the FOT is much more reliable. Second, the FOT is so thick (55 mm) that the overwhelming majority of incident X-ray photons passing through the CsI screen are absorbed, and the life of the CCD is extended accordingly. In our experiment, when incident X-ray photons were absorbed by the CsI screen, their energy was converted into isotropic optical photons, which would spread to the surface of the large end of the FOT after the light channeling process in the microcolumnar CsI:Tl film. These photons were guided by the FOT to the CCD, and then converted to electrical signals. Finally, the electrical signals were handled by readout electronics (including a 16-bit ADC) and image processing software on a PC platform.

2.3 Data processing

Based on IEC standards 62220-1 [15] and 61267 [16], the geometrical set-up of the measuring arrangement was as shown in Fig. 2, and the settings of X-ray tube voltage and additional filtration used for the experiments were obtained from the radiation quality series, as shown in Table 1.

The MTF, expressing the spatial resolution of the detector, was measured by the slanted-edge method. A tungsten plate with thickness 1 mm and area 100 mm×75 mm was used to obtain the slanted-edge image, from which the oversampled edge spread function (ESF) was calculated [17]. The oversampled ESF was differentiated to yield the oversampled line spread function (LSF). Finally the MTF was given after a Fourier transformation of the LSF and normalization using

Table 1. Radiation qualities specified in IEC 62220-1.

radiation quality No.	approximate X-ray tube voltage/kV	half-value layer (HVL)(mm Al)	additional filtration(mm Al)	$SNR^2_{in}1/(mm^2\cdot\mu Gy)$
RQA 3	50	4.0	10.0	21759
RQA 5	70	7.1	21.0	30174
RQA 7	90	9.1	30.0	32362
RQA 9	120	11.5	40.0	31077

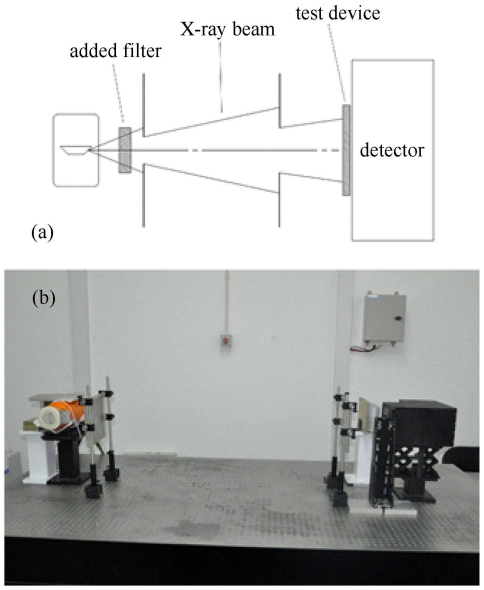

Fig. 2. (a) Geometry of apparatus, based on standards IEC 62220-1 and IEC 61267. (b) All devices were installed on the same optical platform.

Eq. (1):

$$\mathrm{MTF}(u)=\frac{\mathrm{FFT(LSF)}}{\mathrm{FFT(LSF)}|_{u=0}}, \tag{1}$$

where FFT is the digital fast Fourier transform and u is the spatial frequency.

The two dimensional (2D) NPS, expressing the noise variance spectral decomposition of the flat-field image, was calculated using Eq. (2):

$$\mathrm{NPS}(u,v)=\frac{\Delta x\Delta y}{M\cdot 256\cdot 256}\sum_{m=1}^{M}|\mathrm{FFT2}(I(x,y)-S(x,y))|^2, \tag{2}$$

where FFT2 is the two dimensional digital fast Fourier transform, $\Delta x\Delta y$ is the pixel spacing in the horizontal and vertical directions, respectively, M is the number of ROIs, $I(x,y)$ is the pixel value, and $S(x,y)$ is the optionally fitted two-dimensional polynomial. For each flat-field image, a region in the center with 2048×2048 pixels was used. In this region, half-overlapping ROIs with a size of 256×256 pixels, summing up to 225 ROIs, were taken for calculation. After converting 2D NPS to 1D NPS [15], the NNPS is given by Eq. (3):

$$\mathrm{NNPS}(u)=\frac{\mathrm{NPS}(u)}{\mathrm{MPV}^2}, \tag{3}$$

where MVP is the mean value of the pixels used in the calculation of NPS.

DQE is one of the most important metrics to evaluate the overall imaging property of a detector because it can be expressed as the transfer efficiency of signal to noise ratio (SNR) from the input to the output, as shown in Eq. (4):

$$\mathrm{DQE}=\left(\frac{\mathrm{SNR_{out}}}{\mathrm{SNR_{in}}}\right)^2. \tag{4}$$

This means that a lower radiation dose, which implies fewer incident X-ray photons, is required for a higher DQE detector to obtain the same image quality. DQE was determined from entrance surface air Kerma (ESAK), MTF and NNPS using Eq. (5):

$$\mathrm{DQE}(u)=\frac{\mathrm{MTF}^2(u)}{K_a\cdot\mathrm{SNR}^2_{in}\cdot\mathrm{NNPS}(u)}, \tag{5}$$

where K_a is ESAK and SNR^2_{in} is the squared SNR per ESAK of corresponding RQA, as given in Column 5 of Table 1. The ESAK was measured by a diagnostic ion chamber (PTW DIADOS E) connected to the corresponding dosimeter (PTW UNIDOSE E). For each image, the corresponding ESAK was measured using Eq. (5).

3 Results and discussion

3.1 MTF

Figure 3 shows the measured MTF curves of CsI screens with various thicknesses under different radiation qualities. In the medium spatial frequency range (1–6 lp/mm), which is shown in Fig. 4, it is obvious that MTF under RQA5 decreases as a function of CsI screen thickness, which is also observed under RQA3, RQA7 and RQA9. As reported in another study [12], the spatial resolution of a thicker CsI screen is reduced due to lateral light scattering and spreading.

Although the differences between the MTF curves of CsI screens with various thicknesses are significant in the medium spatial frequency range, their MTFs in the lower spatial frequency range (0–1 lp/mm) are very similar. We speculate that the most probable influence is the protective film coating the top surface of the CsI screen. The protective film was located between the large end of the FOT and the microcolumnar CsI:Tl film in the experiment, so the optical photons had to pass through

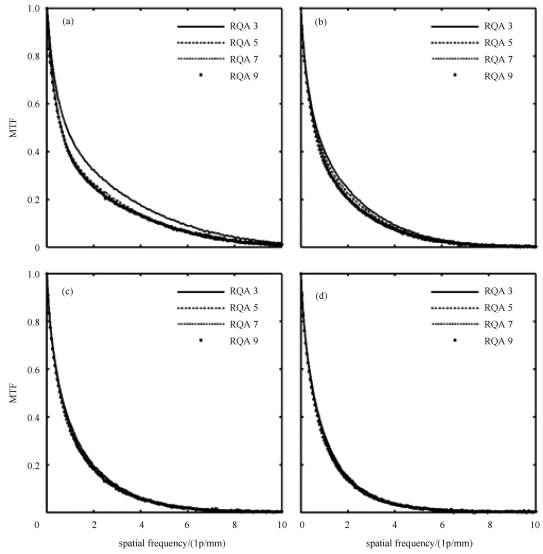

Fig. 3. MTF curves of CsI screens of thickness: (a) 50 μm; (b) 100 μm; (c) 200 μm; and, (d) 300 μm.

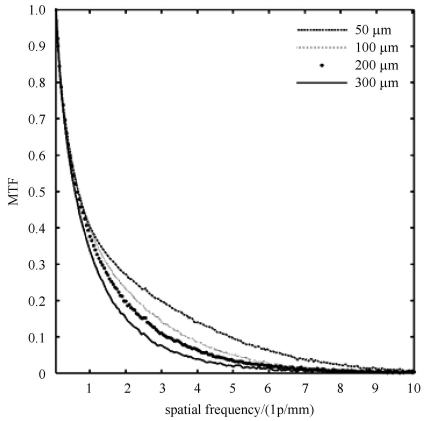

Fig. 4. MTF curves for RQA5 of CsI screens with different film thickness.

the protective film before entering the FOT. In contrast to the channeling process in the microcolumnar CsI:Tl film and FOT, the protective film is isotropic and its MTF is poorer. This explains why the MTF curves of all CsI screen drop similarly, regardless of their thickness. It is important to note that the spatial resolution is influenced by the incident X-ray photon energy. As shown in Fig. 5(a), the MTF curves under RQA3 are significantly higher than those under the other radiation qualities. In Fig. 5(b), the MTF curves under RQA3 are slightly higher than those under the other radiation qualities. In Fig. 5(c) and Fig. 5(d), the differences between MTF curves are negligible. To compare the variation for the same CsI screen thickness, we divided the value of each MTF curve under different radiation qualities by that under RQA3. The result is shown in Fig. 6, from which we can verify that the MTF curves under RQA3 appears higher than those under the other radiation qualities. This phenomenon can be explained by the re-absorption effects of scattering and K-fluorescence [18]. For all the radiation qualities used in this experiment, due to the majority of the incident X-ray photons having energies above the K-edge of Cesium (Cs, 36 keV) and I (Iodine, 33 keV), K-fluorescence plays a role in the image blur. The probability of K-fluorescence and scattering in CsI is summarized in Table 2 [19–21]. This shows that the probability of K-fluorescence and scattering in CsI

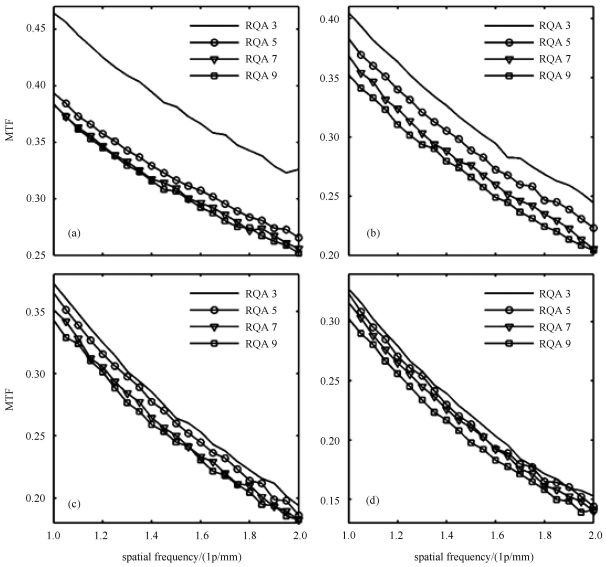

Fig. 5. MTF curves of CsI screens of thickness: (a) 50 μm; (b) 100 μm; (c) 200 μm; and, (d) 300 μm, all for the range 1 to 2 lp/mm.

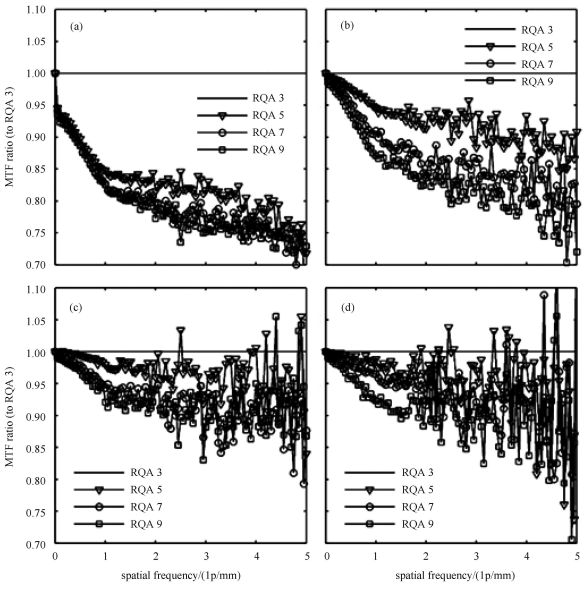

Fig. 6. Ratio of MTF under different radiation qualities to MTF under RQA3 for CsI screens of thickness: (a) 50 μm; (b) 100 μm; (c) 200 μm; and, (d) 300 μm.

Table 2. The probability of K-fluorescence and scattering in CsI.

	Cs		I	
X-ray energy	K-fluorescence	scattering	K-fluorescence	scattering
50 keV	0.737	0.035	0.743	0.037
70 keV	0.741	0.054	0.749	0.058
90 keV	0.745	0.084	0.752	0.089
120 keV	0.746	0.100	0.755	0.108

increases with the incident X-ray photon energy. The mean value of the ratio for medium spatial frequency (2–5 lp/mm) was evaluated and is shown in Table 3. The mean value at higher incident X-ray photon energy is lower than that at lower incident X-ray photon energy. The probability of K-fluorescence and scattering increases with X-ray energy, with the probability at 70 keV, 90 keV and 120 keV being higher by approximately 3%, 6% and 8%, respectively, than that at 50 keV. The maximal difference between radiation qualities is 24%, 20%, 10%, and 10% for 50 μm, 100 μm, 200 μm, and 300 μm, respectively, which means that the energy dependence is distinct for thin CsI screens and negligible for thick CsI screens. For thin CsI screens, more K-fluorescence and scattering X-ray photons escape from the screen, so the proportion of re-absorption effect and blur is lower than that of thick screens.

Table 3. The mean value of the ratio of MTF under different radiation qualities to MTF under RQA3 in the medium spatial frequency range (2–5 lp/mm).

	RQA 3	RQA 5	RQA 7	RQA 9
50 μm	1	0.80	0.76	0.76
100 μm	1	0.91	0.84	0.80
200 μm	1	0.96	0.90	0.91
300 μm	1	0.96	0.92	0.90

3.2 NNPS

Figure 7 shows the NNPS curves under RQA5 at different ESAK. Because the NNPS curves under the other radiation qualities are similar to that under RQA5, their results are not shown. For all CsI screen thicknesses, NNPS decreased as the ESAK increased. Under the same radiation quality, since the number of incident X-ray photons is proportional to ESAK, higher ESAK results in higher SNR at the plane of incidence. For the same CsI screen and optical sensor setting, the system noise caused by CsI screen and optical sensor is invariable, so the overall noise level depends only on ESAK. As ESAK increases, the noise level also increases, but it is relatively low compared to the signal level, causing the SNR to increase.

All the NNPS curves decrease as a function of spatial frequency, but the decline in the higher spatial frequency range (above 8 lp/mm) is slight, except for the 50 μm thick CsI screen. For the 50 μm thick CsI screen, the ESAK varies from 337.7 μm to 1660.9 μm, which is so high that the system noise dominates the overall noise. Since the system noise appears to be spatial frequency dependent, the NNPS curves decrease over the whole spatial frequency range. Conversely, for 100 μm, 200 μm and 300 μm thick CsI screens, the ESAK is relatively low, owing to higher X-ray absorption efficiency. The number of incident X-ray photons, which is proportional to ESAK, is also relatively low and this results in stochastic noise contributing more in the higher spatial frequency range.

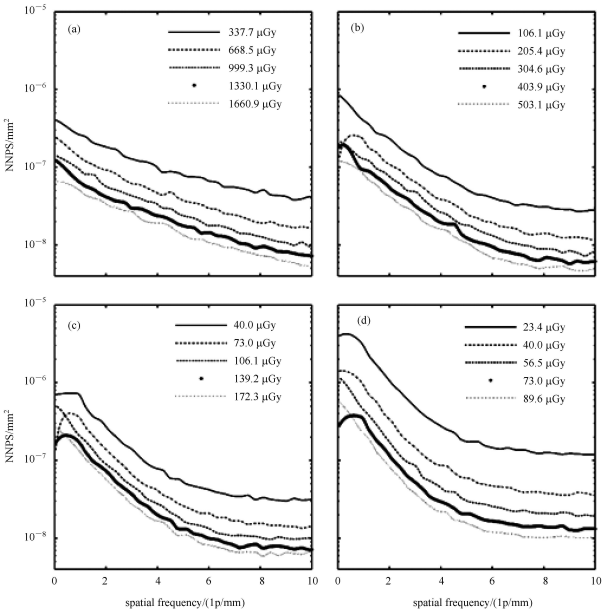

Fig. 7. NNPS curves under RQA5 for CsI screens of thickness (a) 50 μm; (b) 100 μm; (c) 200 μm; (d) 300 μm.

3.3 DQE

Figure 8 shows the DQE curves under different radiation qualities. According to Eq. (5), DQE is determined by ESAK, MTF and NNPS. Since ESAK is constant over the whole spatial frequency range, the features of the DQE curves are determined by the MTF and NNPS curves. Although both the MTF and NNPS decline with spatial frequency, the fall of MTF is faster than that of NNPS. Moreover, according to Eq. (5), DQE is proportional to the square of MTF and only inversely proportional to NNPS. Considering the above two points, the DQE curves, regardless of CsI screen thickness, drop rapidly in the lower spatial frequency range (0–1 lp/mm).

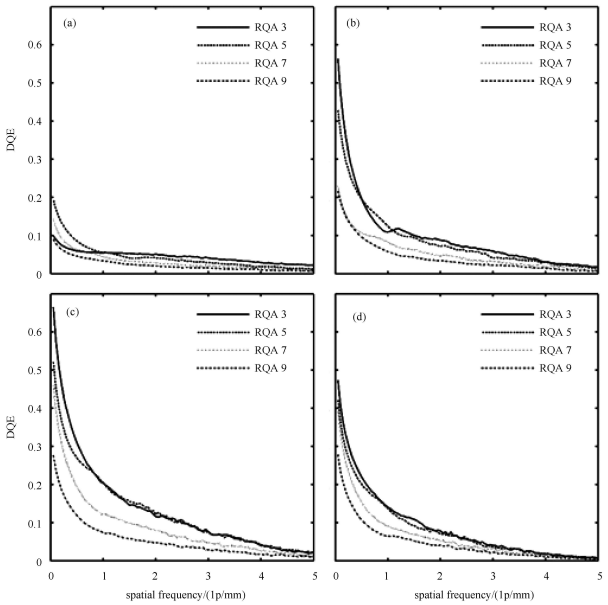

Fig. 8. DQE curves of CsI screens of thickness: (a) 50 μm; (b) 100 μm; (c) 200 μm; and, (d) 300 μm.

Table 4. The maximal value of each DQE curve.

	RQA 3	RQA 5	RQA 7	RQA 9
50 μm	10%	19%	14%	9%
100 μm	56%	43%	23%	22%
200 μm	67%	52%	54%	28%
300 μm	47%	49%	39%	28%

Table 4 shows the maximal value of each DQE curve. For the 50 μm CsI screen, although its MTF curves are highest, its DQE curves are lowest and are no higher than 20%. The microcolumnar CsI:Tl film of the 50 μm CsI screen is too thin to absorb the majority of incident X-ray photons, leading to the number of optical photons emitted by the CsI screen being relatively low compared to the high ESAK. According to Eq. (4), due to the SNR at output being relatively low compared to the SNR at plane of incidence, the DQE of the 50 μm CsI screen is lower than that of thicker CsI screens.

It is also noticeable that for all thicknesses, except 50 μm, the DQE curves under RQA3 and RQA5 are significantly higher than that under RQA7 and RQA9. For the 50 μm CsI screen, only some of the incident X-ray photons are absorbed, so all the DQE curves are very low and close to each other. In contrast, the 100 μm, 200 μm and 300 μm thick CsI screens are thick enough to absorb the majority of incident X-ray photons under RQA3 and RQA5, but only some of those under RQA7 and RQA9. The difference in absorption efficiency causes the DQE curves under RQA3 and RQA5 to be higher. Thus, it can be expected that a higher DQE under RQA7 and RQA9 will be achieved if a CsI screen with thicker film is used to absorb the rest of the incident X-ray photons.

4 Conclusions

In this paper, CsI screens with 50 μm, 100 μm, 200 μm and 300 μm thick microcolumnar CsI:Tl film were prepared and their performances were investigated. Detailed characterizations, in terms of MTF, NNPS and DQE according to IEC 62220-1, have been carried out. The results show that, for the same radiation quality, the MTF of thinner CsI screens is higher than that of thicker ones. The MTF of the same CsI screen was lower when the incident X-ray photon energy was higher, owing to the scattering and K-fluorescence re-absorption effects. The stochastic noise contributed significantly to NNPS in the higher spatial frequency range, while the ESAK decreased. For 100 μm, 200 μm and 300 μm thick CsI screens, the DQE under RQA7 and RQA9 is lower than that under RQA3 and RQA5 due to low absorption efficiency.

References

1 Nagarkar V V, Vasile S, Gothoskar P et al. ApplRadiat Isotopes, 1997, **48**(10–12): 1459–1465
2 Nagarkar V V, Gupta T K, Miller S R et al. IEEE Trans Nucl Sci, 1998, **45**(3): 492–496
3 COSTA E, MASSARO E, PIRO L. Nucl Instrum Methods A, 1986, **243**(2–3): 572–577
4 Coan P, Peterzol A, Fiedler S et al. J Synchrotron Radiat, 2006, **13**: 260–270
5 Lee S C, Kim H K, Chun I K et al. Phys. Med. Biol., 2003, **48**(24): 4173–4185
6 Alberti R, Klatka T, Longoni A et al. X-ray Spectrom, 2009, **38**(3): 205–209
7 Samei E. Med. Phys., 2003, **30**(7): 1747–1757
8 Nagarkar V V, Gaysinskiy V, Ovechkina E E et al. IEEE Trans. Nucl. Sci., 2007, **54**(4): 1378–1382
9 Goertzen A L, Nagarkar V, Street R A et al. Phys. Med. Biol., 2004, **49**(23): 5251–5265
10 Schmitt B, Fuchs M, Hell E et al. Nucl. Instrum Methods B, 2002, **191**: 800–804
11 Marshall N W, Monnin P, Bosmans H et al. Phys. Med. Biol., 2011, **56**(14): 4201–4220
12 ZHAO W, Ristic G, Rowlands J A. Med. Phys., 2004, **31**(9): 2594–2605
13 International Electrotechnical Commission. Medical Electrical Equipment-Characteristics of Digital X-ray Imaging Devices–Part 1: Determination of the Detective Quantum Efficiency. IEC 62220-1, Geneva: IEC, 2003
14 Nikl M. Meas Sci Tecthol, 2006, **17**: 37–54
15 Illers H, Buhr E, Hoeschen C. Radiat Prot Dosim, 2005, **114**(1–3): 39–44
16 International Electrotechnical Commission. Medical Diagnostic X-ray Equipment–Radiation Conditions for use in the Determination of Characteristics. IEC 61267, Geneva: IEC, 1994
17 Marshall N W. Phys. Med. Biol., 2006, **51**(10): 2441–2463
18 Liaparinos P F, Kandarakis I S. Phys. Med. Biol., 2009, **54**(4): 859–874
19 Hubbell J H, Veigele W J, Briggs E A et al. J Phys. Chem. Ref. Data, 1975, **4**(3): 471–538
20 Hubbell J H, Overbo I. J Phys. Chem. Ref. Data, 1979, **8**(1): 69–105
21 Broll N. X-Ray Spectrom, 1986, **15**(4): 271–285